

Characteristics of Current-Induced Harmonic Tremor Signals in Ocean-Bottom Seismometer Records

David Essing^{1,2} , Vera Schlindwein^{*1} , Mechita C. Schmidt-Aursch¹, Celine Hadzioannou² , and Simon C. Stähler³ 

Abstract

Long-lasting harmonic tremor signals are frequently observed in spectrograms of seismological data. Natural sources, such as volcanoes and icebergs, or artificial sources, such as ships and helicopters, produce very similar harmonic tremor episodes. Ocean-bottom seismometer (OBS) records may additionally be contaminated by tremor induced by ocean-bottom currents acting on the OBS structure. This harmonic tremor noise may severely hinder earthquake detection and can be misinterpreted as volcanic tremor.

In a 160-km-long network of 27 OBSs deployed for 1 yr along the Knipovich ridge in the Greenland Sea, harmonic tremor was widely observed away from natural sources such as volcanoes. Based on this network, we present a systematic analysis of the characteristics of hydrodynamically induced harmonic tremor in OBS records to make it distinguishable from natural tremor sources and reveal its generation processes.

We apply an algorithm that detects harmonic tremor and extracts time series of its fundamental frequency and spectral amplitude. Tremor episodes typically occur twice per day, starting with fundamental frequencies of 0.5–1.0 Hz, and show three distinct stages that are characterized by frequency-gliding, mode-locking, and large spectral amplitudes, respectively. We propose that ocean-bottom currents larger than ~ 5 cm/s cause rhythmical Karman vortex shedding around protruding structures of the OBS and excite eigen vibrations. Head-buoy strumming is the most likely source of the dominant tremor signal, whereas a distinctly different tremor signal with a fundamental frequency ~ 6 Hz may be related to eigen vibrations of the radio antenna. Ocean-bottom current velocities reconstructed from the fundamental tremor frequency and from cross correlation of tremor time series between stations match observed average current velocities of 14–20 cm/s in this region. The tremor signal periodicity shows the same tidal constituents as the forcing ocean-bottom currents, which is a further evidence of the hydrodynamic nature of the tremor.

Cite this article as Essing, D., V. Schlindwein, M. C. Schmidt-Aursch, C. Hadzioannou, and S. C. Stähler (2021). Characteristics of Current-Induced Harmonic Tremor Signals in Ocean-Bottom Seismometer Records, *Seismol. Res. Lett.* **XX**, 1–13, doi: [10.1785/0220200397](https://doi.org/10.1785/0220200397).

Supplemental Material

Introduction

Harmonic tremor signals constitute a frequent by-product in seismological records. In contrast to transient and impulsive signals such as earthquakes, long-lasting harmonic tremor is typically identified in spectrograms. Harmonic tremor has a variety of different natural sources, including volcanoes (e.g., Konstantinou and Schlindwein, 2003), icebergs (Müller *et al.*, 2005; Talandier *et al.*, 2006; MacAyeal *et al.*, 2008), glaciers (Helmstetter *et al.*, 2015), and hydrothermal systems (Monigle *et al.*, 2009; Franek *et al.*, 2014), which may produce surprisingly clear tremor signals. However, artificial sources such as rotation of propellers of ships and helicopters or trains (Wilcock *et al.*, 2014; Eibl *et al.*, 2015; Fuchs and Bokelmann,

2017) also produce harmonic tremor signals that are not always easily distinguishable from natural sources. Harmonic tremor signals typically hide their source mechanisms, and a variety of generation processes may produce long-lasting signals with distinct spectra consisting of a fundamental frequency

1. Alfred Wegener Institute, Helmholtz Centre for Polar and Marine Research, Bremerhaven, Germany,  <https://orcid.org/0000-0001-7326-7441> (DE);  <https://orcid.org/0000-0001-5570-2753> (VS); 2. Institute of Geophysics, Center for Earth System Research and Sustainability (CEN), Universität Hamburg, Hamburg, Germany,  <https://orcid.org/0000-0002-5312-2226> (CH); 3. Department of Earth Sciences, ETH Zürich, Zurich, Switzerland,  <https://orcid.org/0000-0002-0783-2489> (SCS)

*Corresponding author: Vera.Schlindwein@awi.de

© Seismological Society of America

and many sharply defined harmonic overtones. For example, rhythmically occurring stick-slip earthquakes as an iceberg moves over ground (MacAyeal *et al.*, 2008) and gas-flux-induced magma oscillations in a volcanic conduit (Jellinek and Bercovici, 2011) may produce harmonic tremor with gliding frequencies. Clues on the underlying source process only come from a detailed analysis of the characteristics of tremor episodes over time.

Harmonic tremor signals in ocean-bottom seismometer (OBS) records have been recognized and described since the beginning of the development of such instruments. Duennebier *et al.* (1981) and Boyd (1984) studied hydrodynamic noise contamination on OBSs that is produced when ocean currents act on the OBS structure and cause Karman vortex shedding. However, in many survey areas, ocean-bottom current velocities remain below the threshold values of ~5–10 cm/s that need to be surpassed to induce hydrodynamic tremor phenomena (Duennebier *et al.*, 1981). OBS surveys in midocean ridge settings frequently report harmonic tremor signals that are often tidally modulated (Monigle *et al.*, 2009; Franek *et al.*, 2014; Meier and Schlindwein, 2018). This type of tremor has typically been attributed to volcanic or hydrothermal processes in the subsurface. Some of these harmonic tremor signals are clearly related in time to the occurrence of earthquake swarms (Meier and Schlindwein, 2018), although tremor appearance is almost indistinguishable from hydrodynamically induced tremor on the OBS structure (Stähler *et al.*, 2018). Recent studies by Stähler *et al.* (2018), Ugalde *et al.* (2019), and Ramakrushna Reddy *et al.* (2020) demonstrate that modern OBS design is also susceptible to substantial hydrodynamic tremor, and previous authors (e.g., Boyd, 1984; Stähler *et al.* (2018)) suggest vortex shedding on protruding structures of the OBS such as the recovery buoy or the flagpole as being the general excitation mechanism. When shedding frequencies match the resonance frequency of the structure, eigen vibrations, in this case head-buoy strumming, are excited, which may amplify the tremor signal. Ugalde *et al.* (2019) observed harmonic tremor in their data set and suggest resonances of the OBS-seafloor coupled system as a source. Spurious harmonic tremor with a fundamental frequency of ~6 Hz was found in several surveys using OBS of the Ocean Bottom Seismic Instrumentation Pool (see Data and Resources) and resulted in an investigation of its sources, but results were inconclusive.

In 2016–2017, we conducted a 12-month OBS survey (Kanzow, 2017; Schlindwein *et al.*, 2017) along the Knipovich ridge in the Greenland Sea (Fig. 1) using 27 OBS from the German Instrument Pool for Amphibian Seismology (DEPAS) (Alfred-Wegener-Institut, Helmholtz-Zentrum für Polar- und Meeresforschung, *et al.*, 2017), to record earthquake activity along this ultraslow spreading midocean ridge (Meier *et al.*, 2021). Records of all OBSs along the 160 km network extent were strongly contaminated by harmonic tremor, including away from locations of known volcanic activity. Extensive

tremor records, different instrumentation within the network, and the comparison of tremor occurrence between stations give a unique possibility to describe in detail the appearance of harmonic tremor in OBS. The purpose of this article is to characterize in detail hydrodynamically induced harmonic tremor on OBSs and to discuss potential generation mechanisms. Thus, an improvement of OBS design is possible, and a distinction between natural and induced tremor is facilitated, avoiding potential misinterpretation of tremor signals.

Method

Instrumentation

We used LOBSTER-type OBS (Fig. 1, top inset) consisting of a Gürdal CMG-40T OBS seismometer (KNR 21: Trillium compact OBS) and a HighTechInc HTI-04-PCA/ULF hydrophone mounted on the frame. Data loggers (SEND Geolon MCS, KNR21: K.U.M. 6D6) sampled the continuous signals at 50 or 100 samples per second. Acoustic release units are situated between syntactic foam buoyancy bodies. To facilitate recovery, the OBS were equipped with a very high frequency radio beacon (Novatec RF-700A1) with a 42-cm-long steel antenna of 1.9 mm diameter mounted together with a Xenon flashlight (Novatec ST-400A) onto the OBS frame. The visibility of the OBS at the sea surface during recovery is further improved by a 1.30–1.40-m-long and 21 mm diameter flagpole that lies horizontally in the water column until the OBS rotates upon release. A head buoy of syntactic foam is attached via a 7–9-m-long and ~18 mm diameter rope to the center of the OBS frame. Typically, two loops divide the rope into roughly even long sections. Four OBS (KNR24–27) reoccupied previous OBS locations for about three weeks in 2017. These were equipped with a Metocean MMB-7500 radio beacon with a shorter antenna of 166 mm length and 10 mm diameter.

Data analysis

Harmonic tremor is typically identified in spectrograms. We remove the instrument response, convert to acceleration, and downsample the data of every station and component to 25 Hz. A band-pass filter is applied between 0.1 and 10 Hz. Then we cut the time series into 80 s time windows and apply a Hann window to avoid edge effects. Fourier transforms are then calculated and plotted sequentially into spectrograms (Fig. 2).

To detect harmonic tremor, we follow the approach of Roman (2017). We expect every spectrum to contain harmonic tremor and estimate first the fundamental frequency f_0 with the Harmonic Product Spectrum (HPS) algorithm (Noll, 1970), taking advantage of the fact that overtone spectral peaks are harmonic multiples of f_0 . The original spectrum is kept, but a copy of it gets decimated by an integer n . The spectral peak of the overtone n in the decimated spectrum is now at the frequency value of the fundamental peak of the uncompressed spectrum. Multiplying the original spectrum by the decimated

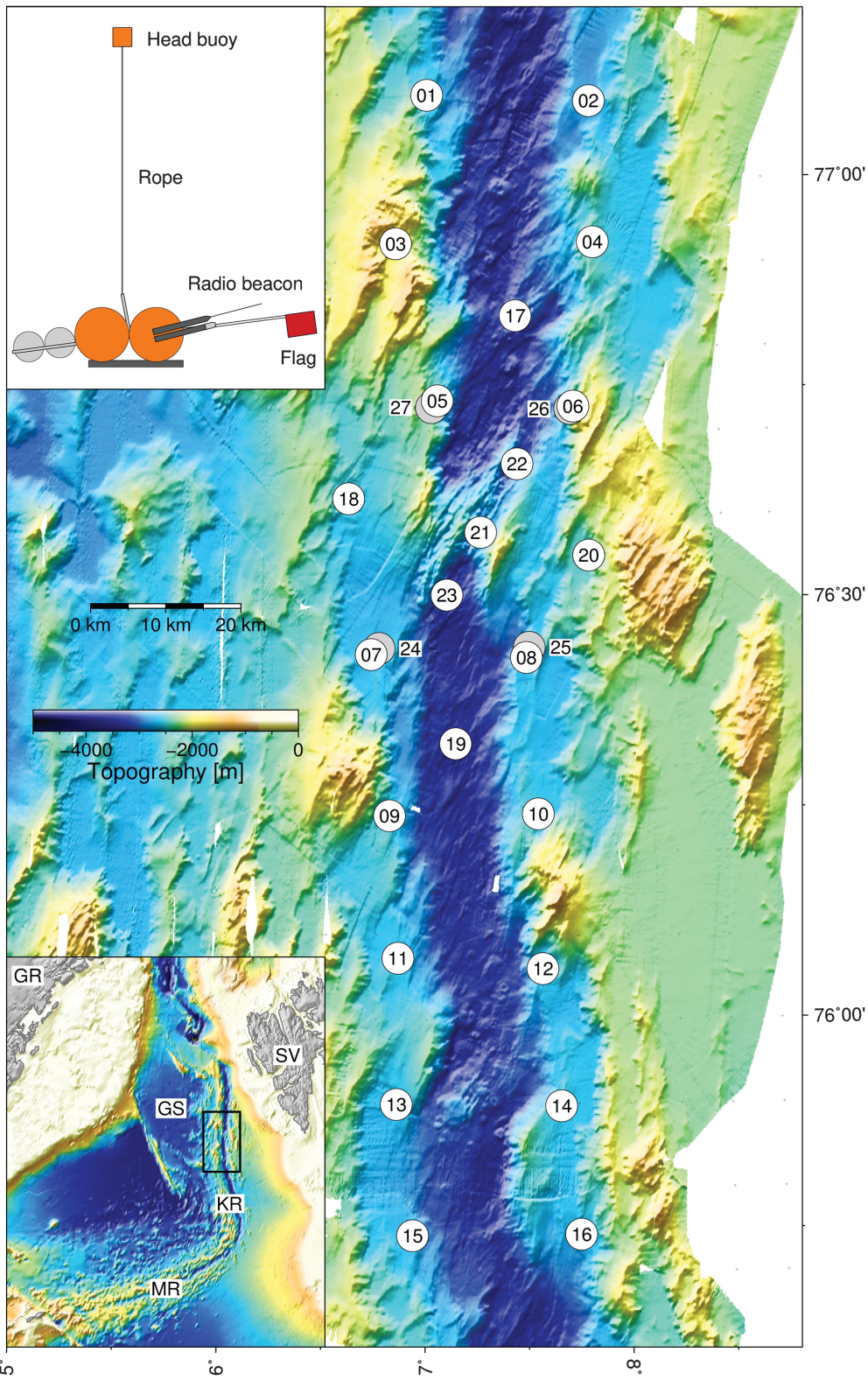


Figure 1. Map of the ocean-bottom seismometer (OBS) positions (white circles) of the KNIPAS network on Knipovich ridge. KNR21 has a different instrumentation. KNR24–27 (gray circles) reoccupied previous OBS locations for a duration of about three weeks. For bathymetry data, see [Data and Resources](#). (Top inset) Sketch (not to scale) of Lobster OBS. (Bottom inset) Overview map of the Greenland Sea. Bathymetry is from the International Bathymetric Chart of the Arctic Ocean (IBCAO) ([Jakobsson et al., 2012](#)). GR, Greenland; GS, Greenland Sea; KR, Knipovich ridge; MR, Mohns ridge; SV, Svalbard.

spectrum leads to an increase of amplitude at f_0 due to coherency, whereas the remaining spectrum is uncorrelated and decreasing in amplitude. This is done for every spectrum calculated before. We tested several values for n and obtained the best results for a value of 4.

We then determined how likely a certain time window contains harmonic tremor. This is done by calculating a ratio between the amplitude at f_0 and the maximum amplitude in the interharmonic part of the spectrum, which is the frequency range between 1.25 and 1.75 times f_0 . We used a threshold ratio of 2, such that harmonic tremor is declared whenever the amplitude of f_0 is twice as large as the maximum amplitude in the interharmonic frequency range. This threshold produced good results in [Roman \(2017\)](#) even if they included several overtones and the related interharmonic part in their estimation. We also tested threshold ratios of 3, which led to unrecognized tremor events, and 1.5, which produced some false tremor detections.

Performance of the harmonic tremor detection algorithm

We applied the described tremor detection algorithm on all stations and all components of the Knipovich Ridge Passive Seismic Network (KNIPAS) for the entire recording period (Fig. 3). Harmonic tremor is more prominent on the seismometer components such that detection by the algorithm tended to work better on these components than the hydrophone. Taking the component of each station where tremor detection worked best

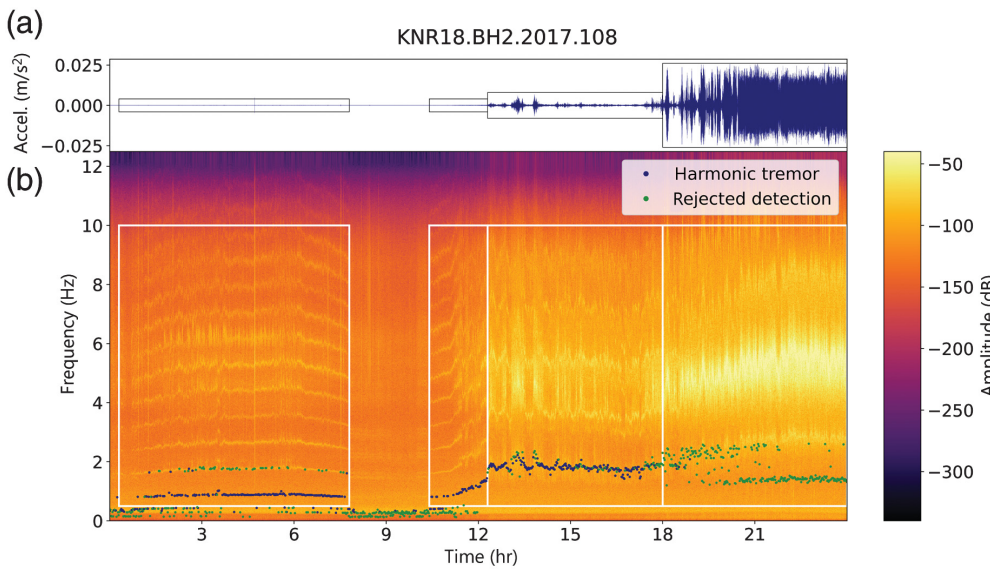


Figure 2. (a) Day seismogram and (b) spectrogram of two tremor episodes. Plot label indicates station, component, year, and Julian day. Weak, intermediate, and strong tremors are marked by boxes of increasing height. Colored dots mark picked values of the fundamental frequency by the tremor detection algorithm showing the classification into correctly and incorrectly identified signals.

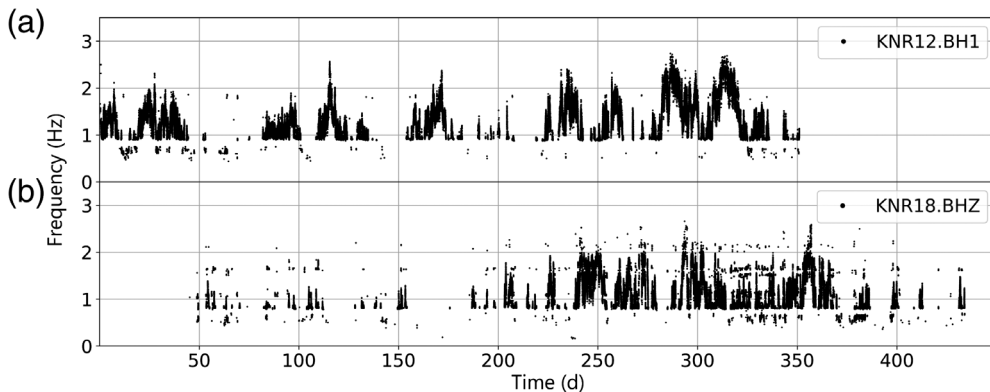


Figure 3. Annual tremor time series for stations (a) KNR12 and (b) KNR18 showing values of the fundamental frequency for each tremor detection. Note that certain frequency levels are absent.

(Table 1), we can identify the precise start and end of harmonic tremor events (Fig. 2). During weak and intermediate tremor events (see the [Harmonic Tremor](#) section), the algorithm is able to detect most of the tremor events. When tremor turns into the strong level, it often lacks well-defined peaks and appears blurry with high noise levels in the interharmonic frequency range such that the amplitude ratio of 2 is not exceeded. Therefore, strong tremor and its f_0 are not always determined precisely (Fig. 2).

Quantifying the ability of harmonic tremor event detection with the HPS algorithm is not trivial because the definition of a sufficiently well-detected event is subjective. We visually inspected all daily spectrograms for components BH2 and BHZ on station KNR18 and for component BH1 on station

KNR12 for tremor occurrence and checked whether the algorithm detected the tremor event. A tremor event was counted as detected when the algorithm classified at least one time window of 80 s as tremor event. For station KNR18, only 5% of the events were not detected on component BHZ, and 13% were not found on component BH2. Component BH1 of station KNR12 had 8% of undetected tremor events. When a harmonic tremor event was correctly detected on all four components, f_0 is the same for all four components. Only the spectral amplitudes differed by 10–20 dB between the seismometer components.

Results

We extracted f_0 and its spectral amplitude whenever the algorithm detected harmonic tremor signals (Fig. 3), and we further visually inspected all daily spectrograms of all stations (e.g., Fig. 2) throughout the survey period to check for the relation of tremor signals to other signals such as the 6 Hz signal discussed subsequently.

Tremor was found on all stations and on all channels, independent of seismometer type. Tremor occurrence at individual stations varied

between 10% and 47% of the time period considered (Table 1), bearing in mind that especially strong tremor was partly not recognized by the algorithm, such that these percentages represent minimum estimates.

f_0 varied mostly (0.5th–99.5th percentile, Table 1) between 0.55 and 2 Hz, the highest value of 2.83 Hz occurring for station KNR06, where tremor was particularly strong. Individual tremor episodes lasted between few hours and several days. Often, two tremor episodes per day could be observed, suggesting some kind of tidal forcing (see the [Tidal Modulation of Tremor and Currents](#) section). With their overtones, tremor signals dominate the frequency band between 1 and \sim 10 Hz (Fig. 2), hindering the phase detection of local earthquakes.

TABLE 1

Harmonic Tremor Occurrence in the Long-Term KNIPAS Network

Station	Chan	% Tremor Occurrence	6 Hz Signal Occurrence	Minimum f_0 (Hz)	0.5% f_0 (Hz)	99.5% f_0 (Hz)	Maximum f_0 (Hz)	Mean f_0 (Hz)	Mean Current Velocity (cm/s)
Western rift flank									
KNR01	BH1	25	–	0.38	0.68	1.88	2.29	1.18	10.1
KNR03	BH1	10	++	0.29	0.50	2.09	2.35	1.11	9.5
KNR05	BH2	47	–	0.31	0.53	1.79	2.16	0.98	8.4
KNR07	BH1	15	+	0.35	0.55	2.14	2.50	1.17	10.0
KNR09	BH1	16	–	0.10	0.38	2.46	2.65	1.34	11.5
KNR11	BH2	32	+	0.16	0.54	2.11	2.55	1.10	9.4
KNR13	BH2	29	–	0.20	0.46	1.80	2.16	0.97	8.3
KNR18	BH2	22	+	0.35	0.54	2.14	2.36	1.17	10.0
Mean		24.5		0.27	0.52	2.05	2.38	1.13	9.7
Eastern rift flank									
KNR02	BH2	26	–	0.31	0.50	1.74	2.01	0.97	8.3
KNR04	BH2	13	–	0.44	0.51	1.50	2.13	0.99	8.5
KNR06	BH1	30	+	0.53	0.56	2.61	2.83	1.74	14.9
KNR08	BH2	47	–	0.46	0.53	1.98	2.21	1.12	9.6
KNR10	BH1	15	++	0.29	0.50	1.98	2.29	0.97	8.3
KNR12	BH1	34	–	0.44	0.66	2.35	2.74	1.37	11.7
KNR14	BH1	37	–	0.23	0.55	1.80	2.10	1.16	9.9
KNR16	BDH	32	–	0.16	0.81	2.31	2.65	1.36	11.7
KNR20	BH1	33	++	0.41	0.80	2.53	2.83	1.48	12.7
Mean		29.7		0.36	0.60	2.09	2.42	1.24	10.6
Rift valley									
KNR17	BH1	14	++	0.25	0.51	1.55	1.95	0.92	7.9
KNR19	BH1	10	++	0.30	0.54	1.79	1.98	0.74	6.3
KNR21	BH1	40	–	0.25	0.51	2.10	2.69	1.10	9.4
KNR22	BH2	43	–	0.18	0.48	1.80	2.43	0.82	7.0
KNR23	BH1	45	++	0.26	0.49	2.08	2.61	1.01	8.7
Mean		30.4		0.25	0.51	1.86	2.33	0.92	7.9
Total mean		28.0		0.31	0.55	2.01	2.36	1.13	9.7

Harmonic tremor occurrence for the channels (Chan) where the tremor detection algorithm performed best and qualitative assessment of 6 Hz signal (–, weak or seldom; +, regular; ++, strong occurrence). Minimum, maximum, and mean values of the fundamental frequency f_0 are given for each station as well as 0.5th and 99.5th percentiles of the f_0 distribution. Current velocities are estimated using a diameter of 1.8 cm of the vortex shedding structure, referring to the head buoy. KNR15 was omitted from this analysis because only the hydrophone channel with limited tremor detection worked.

From the visual inspection, we could identify two different types of tremor signals, which we call here “harmonic tremor” and “6 Hz signal” (Fig. S1, available in the supplemental material to this article). The former is detected

by the harmonic tremor detection algorithm, and the latter is only obvious in the spectrograms. In the following, we describe the characteristic features of both tremor types.

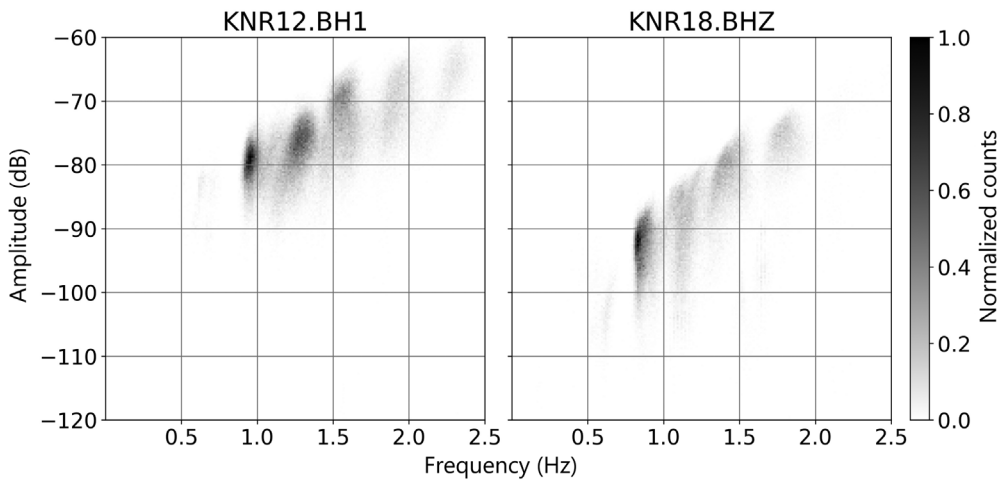


Figure 4. Likelihood of occurrence of fundamental frequency f_0 with their respective spectral amplitude for stations KNR12 and KNR18. Distinct amplitude–frequency combinations occur and amplitude increases with increasing f_0 .

Harmonic tremor

The harmonic tremor signal develops in three different stages that we term weak, intermediate, and strong based on the tremor amplitudes in the seismic traces (Fig. 2) and on spectral characteristics (Fig. S1). The stages are not strictly separable but merge during the evolution of a tremor episode.

Weak tremor. Tremor episodes typically start with weak tremor (Fig. 2, and Figs. S1 and S2) with f_0 around 0.5 Hz and low tremor amplitudes. The spectral lines are sharply defined, and >10 evenly spaced harmonics with similar spectral amplitudes are developed. The tremor displays frequency gliding, with its strictly harmonic character being maintained as the fundamental frequency glides to higher or lower values. Tremor episodes often display a “turtle back” shape, starting with low f_0 and increasing over time and decreasing again (Fig. 2, left). Alternatively, f_0 may further increase until intermediate and eventually strong tremor develops (Fig. 2, right). Tremor episodes fade with weak tremor of decreasing f_0 .

Intermediate tremor. With increasing tremor strength, f_0 no longer varies smoothly as during weak tremor but shows distinct frequency levels that remain constant over time. Tremor may jump back and forth between these distinct frequency levels. Spectral lines are not as sharp as for weak tremor, and typically the first overtone between 3 and 4 Hz exhibits the highest spectral amplitude (Fig. S1). Figure 4 shows a distinct relation between tremor frequency and amplitude. Generally, amplitudes increase with increasing tremor frequency, but certain tremor frequencies are absent (see also Fig. 3). Instead, tremor locks in into preferred frequencies such that discrete patches develop (Fig. 4). These preferred and absent frequencies are the same for all components of one

OBS, but they differ between stations. The spectrograms (Fig. S3) show that these discrete stages are maintained for some time during the evolving tremor episode. This behavior is called mode locking and is typically caused by interaction of a tremor-generating flow mechanism with a resonating structure (e.g., [Sumer and Fredsøe, 1999](#)). [Matoza et al. \(2010\)](#), for example, observed this phenomenon for infrasonic tremor on volcanoes and discussed several physical realization mechanisms.

Strong tremor. The transition to strong tremor is marked

by further increasing f_0 , typically to >2 Hz. Again, the first overtone shows the highest spectral amplitude, but frequencies of this overtone are now between 5 and 6 Hz (Fig. S1). In the time domain, high amplitudes are distinctive for strong tremor episodes and clearly mark the transition from an intermediate tremor stage. Strong tremor may last for entire days (Fig. S4). Mode locking is no longer observed; f_0 continuously varies in an interval of about 0.5 Hz width such that spectral lines are blurred.

6 Hz signal

The 6 Hz signal clearly differs from the harmonic tremor (Fig. 5). The frequency of the 6 Hz signals remains constant over time, occupying a frequency band between about 5.9 and 6.8 Hz (Fig. S5) with a sharply defined upper limit around 6.8 Hz. These frequencies are remarkably stable between stations, differing by $<\sim 0.2$ Hz. One harmonic overtone, at a frequency of 11.8–13.6 Hz, is seen (Fig. S5).

The 6 Hz signal is mostly seen together with weak harmonic tremor. Not all weak tremor episodes are accompanied by a 6 Hz signal. The 6 Hz signal occurs in rare cases independently of harmonic tremor or at least precedes its onset (Fig. 5). As f_0 of the harmonic tremor signal increases, the frequencies in the 6 Hz band move to its upper limit. It appears that with further increasing f_0 of the harmonic tremor, the 6 Hz signal is no longer excited rather than being overprinted by intermediate tremor (Fig. 5). During periods of strong harmonic tremor, the 6 Hz signal is not visible.

About nine stations show a pronounced 6 Hz signal, but the quantification of the occurrence of this signal is difficult because it interferes with the harmonic tremor signal and cannot easily be isolated. However, there is a clear difference in the occurrence of this signal between stations. KNR01, for

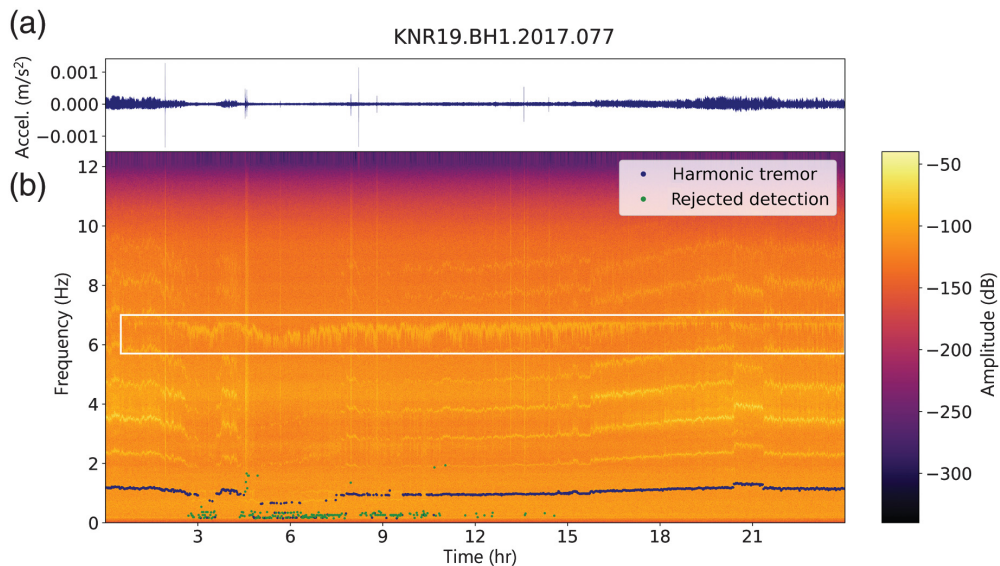


Figure 5. The 6 Hz signal (white box) preceding (hr 5–8) and accompanying (hr 8–16) weak tremor. The 6 Hz signal moves to a sharp upper limit of ~6.8 Hz during increasing fundamental frequencies of intermediate tremor (hr 16–24).

example, hardly displays 6 Hz signals, whereas KNR19 frequently exhibits strong 6 Hz signals, exceeding in amplitude the harmonic tremor signal. A consistent relation to the orientation of the OBS toward the north-south-trending rift valley could not be established for two reasons: (1) OBS orientations were determined from *P*-wave polarization of teleseismic earthquakes (Scholz *et al.*, 2017), but failure of components and partly poor quality of *P*-phase arrivals left orientations uncertain and (2) the intensity and the frequency of occurrence of the 6 Hz signal could only be assessed subjectively (Table 1). However, on a qualitative basis, we found that stations KNR19, KNR23, and KNR17, with the long axis of the OBS oriented obliquely (52°–60°) (see orientation vectors in Fig. 6) to the north-south-trending rift valley (Fig. 1), exhibit particularly frequent and strong 6 Hz signal. Station KNR22, in contrast, in a similar position but oriented at 19° more parallel to the rift valley hardly showed any incidence of the 6 Hz signal, so it appears that the noise is stronger when the flag and radio beacon are perpendicular to the valley. The long axis of the OBS holds the flagpole and the radio beacon (Fig. 1).

We further observe that the 6 Hz signal occurs independently of seismometer and recorder type. Station KNR21 was equipped with both a different seismometer and a different data logger. It showed strong harmonic tremor over extended time periods, and on rare occasions, the 6 Hz signal can be identified. Likewise, the 6 Hz signal is seen occasionally also on the hydrophone channel. This indicates that neither data loggers or seismic sensors are likely sources of the 6 Hz signal.

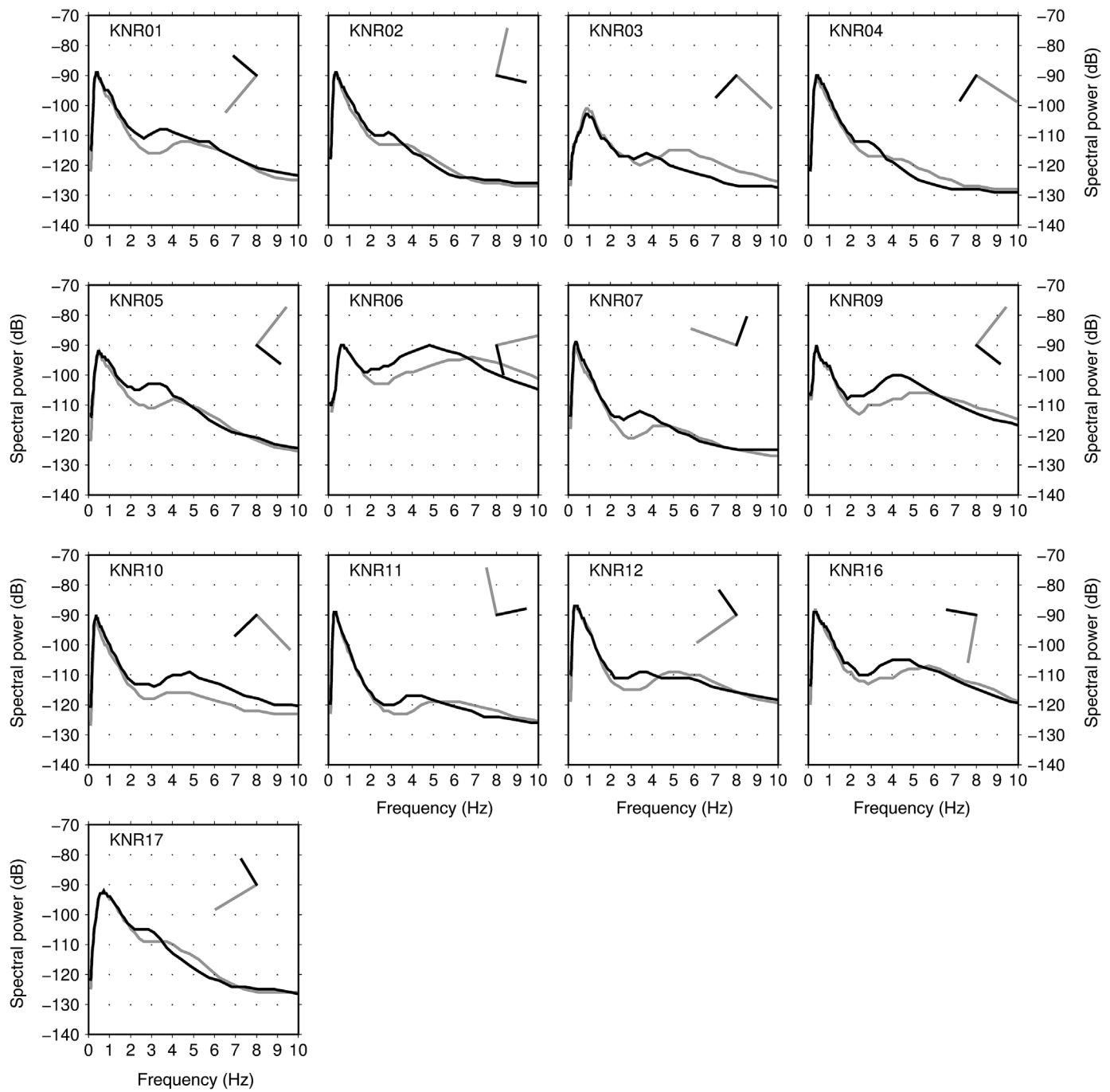
Interpretation and Discussion

Sources of harmonic tremor

Stähler *et al.* (2018) tested two DEPAS OBSs with different seismometers in a shallow water deployment next to an oceanographic mooring equipped with an acoustic doppler current profiler. They suggest that the head buoy on a 7–9 m rope produces the harmonic tremor signals. Camera observations showing head-buoy strumming or comparative measurements of collocated OBSs with and without a head buoy are not available to prove this hypothesis. However, we argue in the following that the observed tremor characteristics may best

be explained by head-buoy strumming.

We propose that weak tremor is excited by shedding of Karman vortices around the rope at frequencies of ~0.5 Hz, somewhat above the fundamental frequency of head-buoy strumming estimated to be <0.48 Hz by Stähler *et al.* (2018). Shedding acts rhythmically on the rope that is directly attached to the OBS frame. The fundamental frequency f_0 smoothly shifts as current velocities increase. Intermediate tremor sets in when the current speed increases the shedding frequency f_0 toward the first overtone of rope oscillations. Mode locking occurs as the tremor is now additionally excited by the resonance of the rope, and a nonlinear coupled system consisting of flow-phenomenon and resonator forms (e.g., Sumer and Fredsøe, 1999). Several stages of this coupled system exist and the tremor appears to flip between those depending on current velocity. As current velocities further increase, strong tremor develops. Mode locking is not as pronounced, and f_0 varies over time such that we suggest that the flow-induced tremor generation dominates over the resonance of the coupled system. We inspected particle-motion diagrams and performed a polarization analysis to test whether these modes act on a particular seismometer component. However, the results did not reveal a clear preferential direction. We compared the median spectral power of the two horizontal components (Fig. 6) obtained from probabilistic power spectral density (PPSD) analysis (McNamara and Buland, 2004). We observe that for the 3–4 Hz interval, where the first overtone of intermediate tremor produces its largest amplitudes, the BH2 component shows a larger spectral power than the BH1 component. This means that in this frequency range, more motion occurs along the short axis of the OBSs. A broad spectral peak between



4 and 6 Hz, potentially excited by strong tremor, is more pronounced on the BH1 component, the long axis of the OBS frame. We suggest that this is an expression of different mode and resonance stages of the coupled flow-induced resonance system. We cannot resolve any details because the coupled system of head buoy and rope is complicated; the tension on the rope and the orientation of rope and head buoy in the water column depend on current direction and velocity.

Bottom currents are expected to act on any elongated, protruding structure of the OBS, such that the same physical mechanism—rhythmic vortex shedding that excites eigen vibrations—may also generate tremor at the flagpole.

Figure 6. Yearly median spectral power on the BH1 (gray) and BH2 (black) seismometer component. OBS orientations toward north (up) are shown with L-shaped symbols, with the long axis representing BH1 (gray). Power is larger on the BH2 component at 3–4 Hz and vice versa at higher frequencies. Only stations with good performance of both horizontal seismometer components are shown evidenced by equal spectral power of both components in the microseismic noise band below 1 Hz.

With its smooth surface, a free length of 1.30–1.40 m and a diameter comparable to the rope, the flagpole appears a likely source of Karman vortex shedding and thereby excited

eigen vibrations. Because the flagpole is firmly mounted in prolongation of the long axis of the OBS (BH1), eigen vibrations of the flagpole are expected to cause stronger motion on the vertical and BH1 channel of the seismometer than on the BH2 channel. Such a behavior could explain the increased spectral power of BH1 relative to BH2 in the frequency band between 4 and 6 Hz (Fig. 6).

However, the following observations suggest that the flagpole is unlikely to represent the dominant source of the hydrodynamic tremor: The flagpole is situated close to the seafloor (<0.5 m) where bottom currents are likely less than at 7–9 m above the seafloor. Depending on the orientation of the OBS, the flagpole may be sheltered by the OBS structure from the prevailing ocean-bottom currents, or it may be oriented parallel to the current direction, which would prevent vortex shedding. The occurrence of tremor signals generated by the flagpole should therefore strongly depend on the station orientation. Bottom currents are preferentially oriented along the rift axis trapped by flanks or ridges as observed, for example, along the Juan de Fuca ridge (Garcia Berdeal *et al.*, 2006) or retrieved in models (Lavelle, 2012; Ruan and Callies, 2020). Harmonic tremor as such and the same distribution of spectral power between the seismometer horizontal components is observed on all OBSs regardless of orientation relative to the assumed current direction.

Because no pronounced effect of the OBS orientation on the tremor signal was seen, we propose that the head buoy rather than the flagpole is the source of the tremor signal. The head buoy rises subvertically from the OBS and is attached with a loop of rope onto the central bar of the OBS (Fig. 1) such that it can move in the current direction, independent of OBS orientation. Given this loose connection between recovery rope and the OBS frame, it is still surprising that the tremor signal couples so effectively into the seismometer.

The preliminary analysis of a seismic experiment at the southern end of Knipovich ridge further supports the hypothesis that head-buoy strumming is the dominant source of the harmonic tremor (Fig. S6). In this experiment, the head buoys of three OBSs were fixed to the OBS frames and were only unfolded upon release such that there was no freely moving rope during the experiment. None of these OBSs showed harmonic tremor, whereas three of the remaining five OBS displayed harmonic tremor.

Sources of the 6 Hz signal

The 6 Hz signal has previously been observed on several other experiments (see [Data and Resources](#)), but slightly different signal types have been described (Monigle *et al.*, 2009, Annual Report OCE-0453971, see [Data and Resources](#)). Almost identical signals to the ones presented here were observed during an active seismic experiment on short-period OBS of the Scripps Institution for Oceanography (SIO; Alaska Langseth Experiment to Understand the Megathrust (ALEUT), see [Data and Resources](#)) and in the

Canary Islands (Ugalde *et al.*, 2019). Because our DEPAS OBSs differ both in instrumentation and frame design from SIO OBSs, we exclude seismometers, data logger, hydrophone, and OBS frame as sources. However, the same type of radio beacon was installed for both SIO OBS experiments and on our OBS (SIO OBS; see [Data and Resources](#)). Duennenbier *et al.* (1981) already suggested radio beacon antennae as possible sources. By modifying the antennae, they could change the resonant frequency but not prevent the excitation of the signal.

Our new data clearly distinguish the 6 Hz signal from the harmonic tremor, pointing to at least two different sources. Because the 6 Hz signal occurs at the same time as the harmonic tremor signal, we can use the latter to estimate the prevailing current velocities following Stähler *et al.* (2018). At station KNR19 (Fig. S4), the relation between both signals is most clearly observed. When 6 Hz tremor sets in, the harmonic tremor shows a f_0 of the order of 0.8–0.9 Hz. With a Strouhal number St of 0.21, the current velocity v is estimated from $v = \frac{fD}{St}$ as 6.9–7.7 cm/s, assuming a diameter D of the rope of 18 mm. This means that vortex shedding at a frequency of 5.9–6.0 Hz should be generated by a structure of 2.2–2.7 mm in diameter. This clearly favors the radio beacon antenna as a potential source, although the antenna has a slightly smaller diameter of 1.9 mm.

Antenna vibrations caused by Karman vortex shedding alone, however, appear too weak to couple into the OBS frame and produce a notable signal. We do not observe smoothly increasing tremor frequencies with increasing current velocity as during turtle-back-shaped weak harmonic tremor. Instead, the 6 Hz signal only sets in in a well-defined frequency band between 5.9 and 6.8 Hz. We suggest that this is an effect of mode locking: when the vortex shedding frequency reaches the eigenfrequency of the antenna, vortex shedding vibrations are amplified by the resonance of the antenna and become strong enough to effectively couple into the OBS frame causing the 6 Hz signal on the seismometer channels. With further increasing current velocities, the shedding frequency exceeds the frequency of the resonance band of the antenna and can no longer excite its resonance. We argue that this effect causes the sharp upper frequency limit of the 6 Hz signal. We cannot readily explain why the resonance frequencies of the antenna occupy a spectral band of 0.9 Hz width rather than yielding a sharply defined spectral line. We speculate that resonance oscillation of the antenna and vortex shedding strongly interact in this frequency band. Although eigen vibrations of the antenna are necessary to amplify the vortex shedding vibrations for the 6 Hz signal to become detectable, they cannot explain its observed integer overtone at \sim 11.8–13.6 Hz because higher resonance modes of an antenna pole fixed at one end are not integer harmonics of the fundamental frequency. The observed integer harmonic must be an effect of the rhythmic vortex shedding vibrations.

The DEPAS instrument pool now uses a new design of radio beacon antenna with a considerably shorter, thicker antenna.

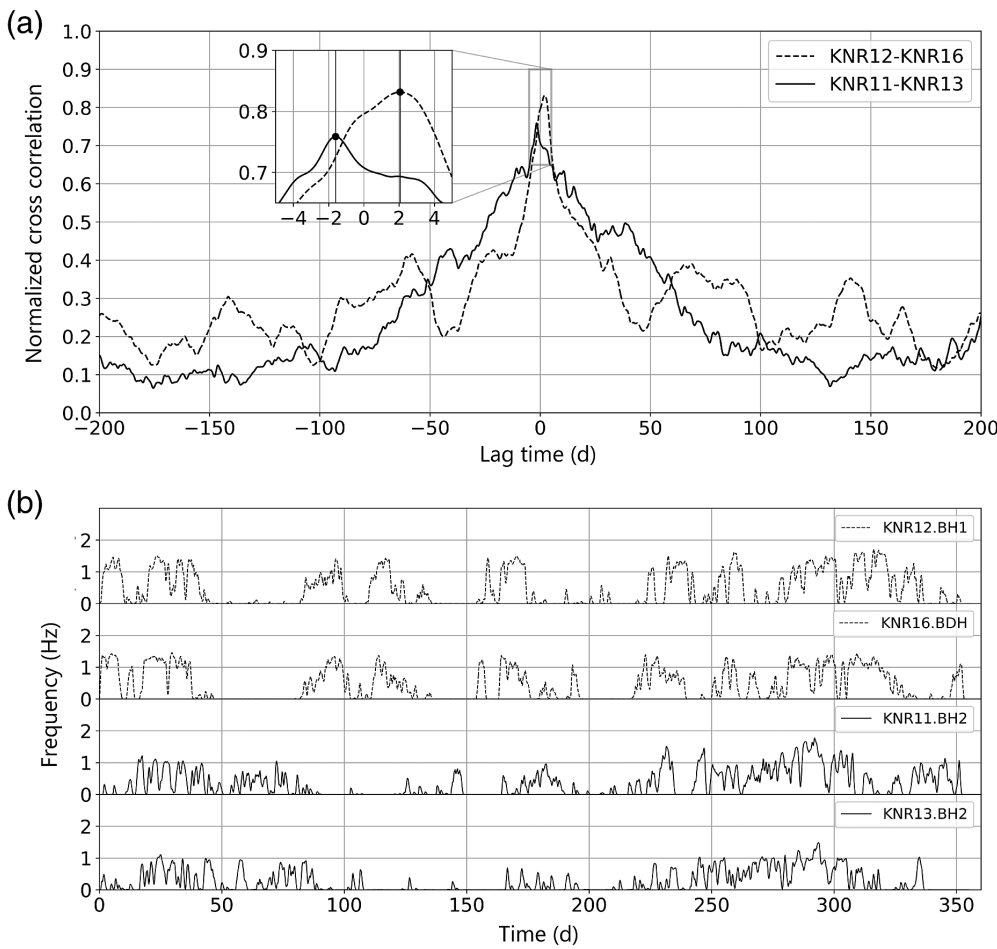


Figure 7. (a) Cross correlation of annual tremor time series shown in (b) between station pairs KNR12 and KNR16 and KNR11 and KNR13. Inset in (a) shows the correlation maximum with positive time lag between KNR12 and KNR16 referring to a northward current and negative time lag between KNR11 and KNR13.

Stations KNR24-27, deployed for a period of three weeks, were equipped with the new radio beacons. Two of these stations showed harmonic tremor as a sign for sufficiently high current velocities, but none of the stations displayed a 6 Hz signal. However, periods of about three weeks without a 6 Hz signal were also observed for stations using the old antenna design, so we cannot give a conclusive answer whether the radio beacon antenna produces the type of 6 Hz signal observed in our and some other data sets.

Velocities of ocean-bottom currents

Harmonic tremor signals typically exhibit about 0.55 Hz as lowest f_0 (Table 1, 0.5th percentile). Some lower values occur (Table 1, min f_0), but stable tremor develops at around this frequency. Because weak tremor is not affected by mode locking, we can use the linear relationship $v = \frac{fD}{S_f}$ to estimate the velocity threshold for tremor excitation. Assuming D to be 1.8 cm, the diameter of the rope, we get an estimate of 4.7 cm/s for the current velocity necessary to generate tremor.

During strong tremor episodes when mode locking no longer occurs, f_0 may reach values of on average 2 Hz (Table 1, 99.5% f_0) with maximum frequencies as high as 2.8 Hz, suggesting peak current velocities of 17 cm/s to a maximum of 24 cm/s. We calculated the mean current velocity at each station (Table 1) from the observations of the mean f_0 , bearing in mind that this omits all phases with lower current velocities that do not excite tremor, and it also skips phases of especially strong bottom currents that excite strong tremor that is not detected by the algorithm. On the eastern rift valley, tremor occurs in 24.5% of the examined time windows with a mean velocity of 9.7 cm/s. The rift valley in contrast has a higher detection rate of tremor (30.4%) but lower velocities (7.9 cm/s), probably related to weak and intermediate tremor that is better detected. For stations such as KNR06 with frequent strong tremor, the algorithm only detected tremor in 30% of the time windows but current

velocities are on average 14.9 cm/s.

We observed that annual f_0 time series at neighboring stations KNR12, KNR14, and KNR16 at the eastern rift flank and stations KNR11 and KNR13 at the western rift flank showed similar patterns on the scale of weeks (Fig. 7b). We calculated the cross correlation of the f_0 time series between stations (Fig. 7). The cross correlation of the f_0 time series of KNR11 with KNR13 yielded a correlation maximum of 0.76 at a time lag of -1.60 days, with the tremor signal appearing first on the northern station KNR11. Between stations KNR12 and KNR16, the cross correlation reached a value of 0.83 at a time lag of 2.05 days, with the tremor signal appearing first on the southern station KNR16. Using the station distance, we can infer mean velocities of bottom water masses of ~14 cm/s in southward direction along the western rift flank and 20 cm/s northward along the eastern rift flank. The directions match observations by Walczowski *et al.* (2005), who studied volume transport in the complex West Spitsbergen current system. They observed a net northward

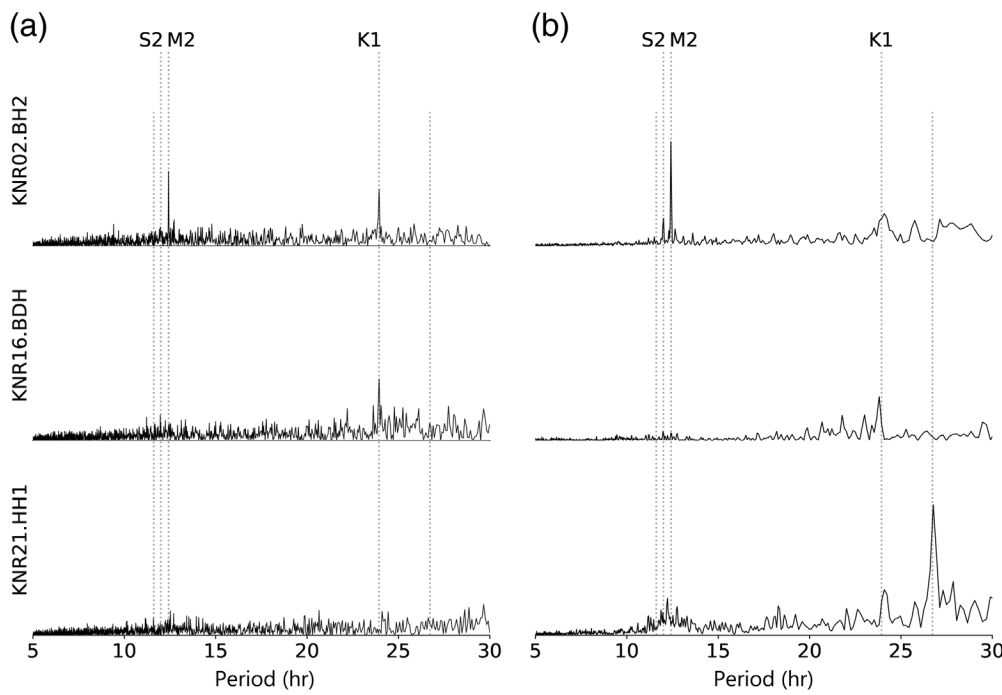


Figure 8. (a) Tidal analysis of annual tremor time series of f_0 and (b) median spectral power in the frequency band 0.5–3.1 Hz for stations KNR02, KNR16, and KNR21. Spectral amplitudes (vertical axes) are normalized for comparison. Theoretical tidal constituents are marked by dotted lines and labeled. Major constituents M2, S2, and K1 are discussed in the [Tidal Modulation of Tremor and Currents](#) section and in Table S1.

mass transport along the eastern rift valley flank of Knipovich ridge and a southward transport along its western flank, but our annual current velocity estimates exceed their measured values of a snapshot observation in July 2003. Current velocities estimated from cross-correlation annual tremor time series are also slightly higher than mean velocities derived from f_0 (Table 1: 11.7 cm/s at stations KNR12 and KNR16), but mode locking and lack of detection of strong tremor lead to underestimated values. Measured mean velocities of [von Appen et al. \(2017\)](#) in a slightly different topographic setting ~200 km north of our OBS network suggest mean bottom current velocities of 15.6 cm/s. Our estimates using tremor f_0 and cross correlations of annual tremor f_0 time series thus correctly reproduce the order of magnitude and direction of prevailing ocean-bottom currents along Knipovich ridge.

Tidal modulation of tremor and currents

To examine the periodicity of the detected hydrodynamic tremor, we transformed the f_0 time series over the duration of the experiment into the frequency domain using the component that produced the best tremor detection. In addition, we analyzed PPSDs calculated at 15 min intervals. We submitted the time series of the mean spectral power in the frequency range between 0.5 and 3.1 Hz containing f_0 to the same Fourier analysis. Figure 8 shows the computed Fourier spectrum of

both time series for stations KNR02, KNR16, and KNR21 along with tidal constituents. Both methods produce comparable results that vary only in amplitude of the spectral peak but not in periodicity. The most prominent tidal constituents are the Principal Lunar Semidiurnal M2 (12.42 hr), the Principal Solar Semidiurnal S2 (12 hr), and the Lunar Diurnal K1 (23.93 hr); at least one of them is found on 18 stations (Table S1). This is in good agreement with direct measurements of [Poulain and Centurioni \(2015\)](#), who found substantial tidal currents in the northwestern Barents Sea and south of Svalbard, in particular with a periodicity of the semi-diurnal M2 and the diurnal K1 tide. Comparing tidal constituents over the seismometer network (Table S1), we find higher amplitudes for the M2 tide on the stations in the

northern part of the network (KNR01, Fig. 8). For comparison, we conducted a spectral analysis of current velocity data ([von Appen et al., 2017; Salter et al., 2018](#)) collected a few meters above the ocean bottom by moorings deployed 200 km north of stations KNR01 and KNR02. We also found a prominent M2 tidal constituent. In contrast, stations in the southern part of the network (KNR16, Fig. 8) are more affected by the K1 tide, in agreement with model calculations of [Gjevik and Straume \(1989\)](#), who found diurnal tidal constituents dominant in the vicinity of Bear Island south of Svalbard. Tremor on five OBS stations is not modulated by tides. These stations (e.g., KNR21, Fig. 1) are found predominantly in the center of the KNIPAS network, where a major volcanic edifice produces a bathymetric obstacle that may affect tidal currents. Although the West Spitsbergen current system running parallel to Knipovich ridge constitutes a prominent regional current system ([Walczowski et al., 2005](#)), [Ramakrushna Reddy et al. \(2020\)](#) show that internal ocean tides in the Andaman-Nicobar region can also produce pronounced currents that excite strong harmonic tremor on OBS. In their observations, ocean currents and resulting hydrodynamic tremor share the same tidal characteristics. Thus, ocean-bottom currents in a variety of oceanographic settings may be strong enough to excite hydrodynamic tremor in OBS records, and the tremor signals reproduce the current velocities and periodicity of the forcing currents.

Conclusions

We quantitatively analyzed strong harmonic tremor signals in the frequency range of 0.5–10 Hz that contaminated continuous seismic records of an extended network of 27 OBS deployed along Knipovich ridge in the Greenland Sea.

1. Persistent hydrodynamic harmonic tremor is produced by ocean-bottom currents above 4.7 cm/s. Mean bottom current velocities of \sim 9.7 cm/s cause up to 40% of the seismic records to be contaminated by harmonic tremor in the frequency range of 0.5–10 Hz.
2. Hydrodynamic harmonic tremor episodes last for hours and occur typically twice per day. Three distinctive tremor stages can be distinguished. Episodes start with weak tremor with $f_0 \cong 0.5$ Hz and up to 10 harmonic overtones. Frequencies and amplitudes glide to higher values to merge into intermediate tremor that shows distinct frequency levels. Strong tremor has f_0 of about 2 Hz and high amplitudes, and its harmonic character is often blurred. All seismometer components and to a lesser extent the hydrophones are affected. OBS orientation relative to the current direction appears irrelevant. Harmonic tremor is likely being produced by Karman vortex shedding on the head-buoy rope, which excites resonance vibrations of the system.
3. 6 Hz tremor occurs in parallel to weak and intermediate harmonic tremor. It displays a sharply bounded frequency band between 5.9 and 6.8 Hz. It has been observed on different types of OBSs. We speculate that the radio beacon antenna is a likely source.
4. Midocean ridges constitute an environment where ocean-bottom currents are intensified, and threshold velocities of >5 cm/s may regularly be reached, leading to contamination of seismological records with at least weak to intermediate hydrodynamic tremor. Because volcanic or hydrothermal fluid flow may produce harmonic tremor with similar characteristics, careful analysis of tremor properties is vital to avoid confusion. Hydrodynamic harmonic tremor episodes display tidal variations similar to the exciting current systems.

Modifications of the OBS design are desirable for deployments in areas of high bottom current velocities. We are currently testing different radio beacon antennae, a modified head-buoy design that releases the rope only upon recovery, and different flagpole lengths for their effects on contamination of OBS records with hydrodynamically induced tremor.

Data and Resources

Raw ocean-bottom seismometer (OBS) data can be retrieved from the PANGAEA repository (<https://doi.pangaea.de/10.1594/PANGAEA.896635>). Our tremor detection algorithm is released as [Essing et al. \(2021\)](#). The other relevant data were from the following websites: <http://www.obsip.org/data/6hz-noise>, Annual Report OCE-0453971; http://obsip.iris.edu/documents/Y10-Annual-OBSIP-SIO_noise.pdf,

ALEUT: http://www.obsip.org/images/deployment_maps/cruise_report_mgl1110_with_appendices.pdf (pages C-9–C-13, and Scripps Institution for Oceanography (SIO) OBS: <http://www.obsip.org/instruments/short-period/sio/specifications>. All websites were last accessed in July 2020. Bathymetry data of Figure 1 are from data sets <https://doi.pangaea.de/10.1594/PANGAEA.895661>, PANGAEA.895668, PANGAEA.892814, and PANGAEA.892679. The ObsPy package was used for calculating the probabilistic power spectral densities (PPSDs; [Beyreuther et al., 2010](#); [Krischer et al., 2015](#)). Figure 1 was created with Generic Mapping Tools (GMT; [Wessel et al., 2013](#)). Supplemental material for this article includes a table with tidal constituents and six figures with further examples of spectra and spectrograms of the described tremor and 6 Hz signals and the effect of the head buoy on tremor generation.

Declaration of Competing Interests

The authors acknowledge there are no conflicts of interest recorded.

Acknowledgments

The authors acknowledge the crew and scientists of cruises R/V Polarstern PS100 (doi: [10.2312/BzPM_0705_2017](#), Grant AWI-PS100_09) and R/V Maria S. Merian MSM67 (doi: [10.2312/cr msm67](#)) and MSM68 (doi: [10.2312/cr msm68](#)) for their support in the ocean-bottom seismometer (OBS) operations. Instruments were provided by the German DEPAS pool for amphibian seismology (doi: [10.17815/jlsrf-3-165](#)).

References

- Alfred-Wegener-Institut, Helmholtz-Zentrum für Polar- und Meeresforschung, et al. (2017). DEPAS (Deutscher Geräte-Pool für amphibische Seismologie): German instrument pool for amphibian seismology, *J. Large Scale Res. Facil.* 3, no. A122, doi: [10.17815/jlsrf-3-165](#).
- Beyreuther, M., R. Barsch, L. Krischer, T. Megies, Y. Behr, and J. Wassermann (2010). ObsPy: A python toolbox for seismology, *Seismol. Res. Lett.* 81, 530–533, doi: [10.1785/gssrl.81.3.530](#).
- Boyd, J. D. (1984). Currents near deep sea drilling project hole 395A and effects on components of the marine seismic system project, *Deep Sea Drill. Proj. Initial Rep.* 78b, 759–766, doi: [10.2973/dsdp.proc.78b.111.1984](#).
- Duennbier, F. K., G. Blackington, and G. H. Sutton (1981). Current-generated noise recorded on ocean bottom seismometers, *Mar. Geophys. Res.* 5, 109–115.
- Eibl, E. P. S., I. Lokmer, C. J. Bean, E. Akerlie, and K. S. Vogfjord (2015). Helicopter vs. volcanic tremor: Characteristic features of seismic harmonic tremor on volcanoes, *J. Volcanol. Geoth. Res.* 304, 108–117, doi: [10.1016/j.jvolgeores.2015.08.002](#).
- Essing, D., V. Schlindwein, M. C. Schmidt-Aursch, C. Hadzioannou, and S. C. Stähler (2021). Fundamental frequency detection (version v1.0), Zenodo, doi: [10.5281/zenodo.4623340](#).
- Franek, P., J. Mienert, S. Buenz, and L. Géli (2014). Character of seismic motion at a location of a gas hydrate-bearing mud volcano on the SW Barents Sea margin, *J. Geophys. Res.* 119, 6159–6177, doi: [10.1002/2014JB010990](#).
- Fuchs, F., and G. Bokelmann (2017). Equidistant spectral lines in train vibrations, *Seismol. Res. Lett.* 89, 56–66, doi: [10.1785/0220170092](#).

- Garcia Berdeal, I., S. L. Hautala, L. N. Thomas, and H. Paul Johnson (2006). Vertical structure of time-dependent currents in a mid-ocean ridge axial valley, *Deep Sea Res. Oceanogr. Res. Pap.* **53**, 367–386, doi: [10.1016/j.dsr.2005.10.004](https://doi.org/10.1016/j.dsr.2005.10.004).
- Gjevik, B., and T. Straume (1989). Model simulations of the M₂ and the K₁ tide in the Nordic Seas and the Arctic Ocean, *Tellus Dyn. Meteorol. Oceanogr.* **41**, 73–96, doi: [10.3402/tellusa.v41i1.11822](https://doi.org/10.3402/tellusa.v41i1.11822).
- Helmstetter, A., L. Moreau, B. Nicolas, P. Comon, and M. Gay (2015). Intermediate-depth icequakes and harmonic tremor in an Alpine glacier (Glacier d'Argentière, France): Evidence for hydraulic fracturing, *J. Geophys. Res.* **120**, 402–416, doi: [10.1002/2014JF003289](https://doi.org/10.1002/2014JF003289).
- Jakobsson, M., L. Mayer, B. Coakley, J. A. Dowdeswell, S. Forbes, B. Fridman, H. Hodnesdal, R. Noormets, R. Pedersen, M. Rebescu, et al. (2012). The International Bathymetric chart of the Arctic Ocean (IBCAO) version 3.0, *Geophys. Res. Lett.* **39**, doi: [10.1029/2012gl052219](https://doi.org/10.1029/2012gl052219).
- Jellinek, A. M., and D. Bercovici (2011). Seismic tremors and magma wagging during explosive volcanism, *Nature* **470**, 522–526, doi: [10.1038/nature09828](https://doi.org/10.1038/nature09828).
- Kanzow, T. (2017). The expedition PS100 of the research vessel Polarstern to the Fram Strait in 2016, *Rep. Polar Res.* **705**, doi: [10.2312/BzPM_0705_2017](https://doi.org/10.2312/BzPM_0705_2017).
- Konstantinou, K. I., and V. Schlindwein (2003). Nature, wavefield properties and source mechanism of volcanic tremor: A review, *J. Volcanol. Geoth. Res.* **119**, 161–187.
- Krischer, L., T. Megies, R. Barsch, M. Beyreuther, T. Lecocq, C. Caudron, and J. Wassermann (2015). ObsPy: A bridge for seismology into the scientific Python ecosystem, *Comput. Sci. Discov.* **8**, doi: [10.1088/1749-4699/8/1/014003](https://doi.org/10.1088/1749-4699/8/1/014003).
- Lavelle, J. W. (2012). On the dynamics of current jets trapped to the flanks of mid-ocean ridges, *J. Geophys. Res.* **117**, doi: [10.1029/2011jc007627](https://doi.org/10.1029/2011jc007627).
- MacAyeal, D. R., E. A. Okal, R. C. Aster, and J. N. Bassis (2008). Seismic and hydroacoustic tremor generated by colliding icebergs, *J. Geophys. Res.* **113**, doi: [10.1029/2008JF001005](https://doi.org/10.1029/2008JF001005).
- Matoza, R. S., D. Fee, and M. A. Garcés (2010). Infrasonic tremor wavefield of the Pu'u 'O'o crater complex and lava tube system, Hawaii, in April 2007, *J. Geophys. Res.* **115**, doi: [10.1029/2009jb007192](https://doi.org/10.1029/2009jb007192).
- McNamara, D., and R. Buland (2004). Ambient noise levels in the continental United States, *Bull. Seismol. Soc. Am.* **94**, 1517–1527, doi: [10.1785/012003001](https://doi.org/10.1785/012003001).
- Meier, M., and V. Schlindwein (2018). First in situ seismic record of spreading events at the ultraslow spreading Southwest Indian ridge, *Geophys. Res. Lett.* **45**, 10,360–10,368, doi: [10.1029/2018gl079928](https://doi.org/10.1029/2018gl079928).
- Meier, M., V. Schlindwein, J.-R. Scholz, J. Geils, M. C. Schmidt-Aursch, F. Krüger, W. Czuba, and T. Janik (2021). Segment-scale seismicity of the ultraslow spreading Knipovich Ridge, *Geochem. Geophys. Geosys.* **22**, e2020GC009375, doi: [10.1029/2020GC009375](https://doi.org/10.1029/2020GC009375).
- Monigle, P. W., D. R. Bohnenstiel, M. Tolstoy, and F. Waldhauser (2009). Seismic tremor at the 9°50'N East Pacific Rise eruption site, *Geochem. Geophys. Geosys.* **10**, doi: [10.1029/2009gc002561](https://doi.org/10.1029/2009gc002561).
- Müller, C., V. Schlindwein, A. Eckstaller, and H. Miller (2005). Singing icebergs, *Science* **310**, 1299–1299, doi: [10.1126/science.1117145](https://doi.org/10.1126/science.1117145).
- Noll, M. A. (1970). Pitch determination of human speech by the harmonic product spectrum, the harmonic sum spectrum and a maximum likelihood estimate, *Proc. of the Symposium on Computer Processing in Communications XIX*, Polytechnic Press, Brooklyn, New York, 779–797.
- Poulain, P.-M., and L. Centurioni (2015). Direct measurements of World Ocean tidal currents with surface drifters, *J. Geophys. Res.* **120**, 6986–7003, doi: [10.1002/2015jc010818](https://doi.org/10.1002/2015jc010818).
- Ramakrushana Reddy, T., P. Dewangan, L. Arya, P. Singha, and K. A. Kamesh Raju (2020). Tidal triggering of the harmonic noise in ocean-bottom seismometers, *Seismol. Res. Lett.* **91**, 803–813, doi: [10.1785/0220190080](https://doi.org/10.1785/0220190080).
- Roman, D. C. (2017). Automated detection and characterization of harmonic tremor in continuous seismic data, *Geophys. Res. Lett.* **44**, 6065–6073, doi: [10.1002/2017GL073715](https://doi.org/10.1002/2017GL073715).
- Ruan, X., and J. Callies (2020). Mixing-driven mean flows and submesoscale eddies over mid-ocean ridge flanks and fracture zone canyons, *J. Phys. Oceanogr.* **50**, 175–195, doi: [10.1175/jpo-d-19-0174.1](https://doi.org/10.1175/jpo-d-19-0174.1).
- Salter, I., E. Bauerfeind, E.-M. Nöthig, W.-J. von Appen, N. Lochthofen, T. Soltwedel, and I. Schewe (2018). Physical oceanography and current meter data from mooring HG-IV-FEVI-34 at Hausgarten IV, doi: [10.1594/PANGAEA.884543](https://doi.org/10.1594/PANGAEA.884543).
- Schlindwein, V., F. Krüger, F. Schmid, M. Schmidt-Aursch, R. Brune, F. Dorgerloh, F. Elekes, J. Geils, H. Lilienkamp, M. Metz, et al. (2017). KNIPAS Knipovich ridge passive seismic experiment MSM68, *Maria S. Merian Berichte MSM68*, doi: [10.2312/cr_msm68](https://doi.org/10.2312/cr_msm68).
- Scholz, J.-R., G. Barruol, F. R. Fontaine, K. Sigloch, W. C. Crawford, and M. Deen (2017). Orienting ocean-bottom seismometers from P-wave and Rayleigh wave polarizations, *Geophys. J. Int.* **208**, 1277–1289, doi: [10.1093/gji/ggw426](https://doi.org/10.1093/gji/ggw426).
- Stähler, S. C., M. C. Schmidt-Aursch, G. Hein, and R. Mars (2018). A self-noise model for the German DEPAS OBS pool, *Seismol. Res. Lett.* **89**, 1838–1845, doi: [10.1785/0220180056](https://doi.org/10.1785/0220180056).
- Sumer, B. M., and J. Fredsøe (1999). *Hydrodynamics around Cylindrical Structures*, P. Liu (Editor), Vol. 12, Advanced Series on Ocean Engineering, World Scientific, Singapore.
- Talandier, J., O. Hyvernaud, D. Reymond, and E. A. Okal (2006). Hydroacoustic signals generated by parked and drifting icebergs in the Southern Indian and Pacific Oceans, *Geophys. J. Int.* **165**, 817–834, doi: [10.1111/j.1365-246X.2006.02911.x](https://doi.org/10.1111/j.1365-246X.2006.02911.x).
- Ugalde, A., B. Gaite, M. Ruiz, A. Villaseñor, and C. R. Ranero (2019). Seismicity and noise recorded by passive seismic monitoring of drilling operations offshore the Eastern Canary Islands, *Seismol. Res. Lett.* **90**, 1565–1576, doi: [10.1785/0220180353](https://doi.org/10.1785/0220180353).
- von Appen, W.-J., K. Latarius, and T. Kanzow (2017). Physical oceanography and current meter data from mooring F6-17, doi: [10.1594/PANGAEA.870845](https://doi.org/10.1594/PANGAEA.870845).
- Walczowski, W., J. Piechura, R. Osinski, and P. Wieczorek (2005). The West Spitsbergen current volume and heat transport from synoptic observations in summer, *Deep Sea Res. Oceanogr. Res. Pap.* **52**, 1374–1391, doi: [10.1016/j.dsr.2005.03.009](https://doi.org/10.1016/j.dsr.2005.03.009).
- Wessel, P., W. H. F. Smith, R. Scharroo, J. F. Luis, and F. Wobbe (2013). New, improved version of the Generic Mapping Tools released, *Eos Trans. AGU* **94**, 409–410.
- Wilcock, W. S., K. M. Stafford, R. K. Andrew, and R. I. Odom (2014). Sounds in the ocean at 1–100 Hz, *Ann. Rev. Mar. Sci.* **6**, 117–140, doi: [10.1146/annurev-marine-121211-172423](https://doi.org/10.1146/annurev-marine-121211-172423).

Manuscript received 23 October 2020

Published online 28 April 2021